Supporting Information

Cu(I)-cluster-based Covalent Organic Frameworks with Open Metal Sites and Tuned Microporosity for Efficient C_2H_2/CO_2 Separation

Pengyue Hao,[‡a] Jialiang Liu,[‡a] Sen Wang,[a] Shijie Wang,[b] Lulan Xu,[a] Wang Zhang[a] and Yongwu Peng[*a,b]

[a] College of Materials Science and Engineering, Science and Education Integration College of Energy and Carbon Neutralization, Zhejiang University of Technology, Hangzhou 310014, China
[b] School of Materials Science and Chemical Engineering, Ningbo University, Ningbo 315211, China.
E-mail: ywpeng@zjut.edu.cn; pengyongwu@nbu.edu.cn
‡ These authors contributed equally to this work.

Table of Contents

1. Materials and methods

Hexakis(4-aminophenyl)benzene;1,1':2',1''-Terphenyl]-4,4''-diamine, [1,1':4',1'':2'',1''':4''',1''''-Quinquephenyl]-4,4''''-diamine, 1H-Pyrazole-4-carboxaldehyde were purchased from Shanghai Tensus Biotech Co., Ltd. $Cu(NO_3)_2 \cdot 3H_2O$, N, N-dimethylformamide, ethanol, 1-Butanol, N, N-dimethylacetamide (DMA, 99%) were purchased from Tokyo Chemical Industry Co., Ltd., All the materials were used as received without further purification.

Fourier transform infrared (FT-IR): IR spectrum was measured on an IR spectrometer (Nicolet 6700) between the ranges of 4000 to 400 cm^{-1}.

Solid-state nuclear magnetic resonance (ssNMR): Solid-state nuclear magnetic resonance (NMR) data were performed on a Bruker AVANCE III 600 spectrometer with cross-polarization magic-angle-spinning (CP/MAS) at a resonance frequency of 150.9 MHz. ^{13}C CP/MAS NMR spectra were recorded using a 4 mm MAS probe and a spinning rate of 14 kHz. A contact time of 4 ms and a recycle delay of 2 s were used for the ^{13}C CP/MAS NMR measurement. The chemical shifts of ^{13}C were externally referenced to tetramethylsilane (TMS).

X-ray photoelectron spectroscopy (XPS): XPS spectra were collected using a Thermo Scientific ESCALAB 250Xi spectrometer equipped with a monochromatic Al-Kα source.

Thermogravimetric analysis (TGA): TGA was performed using a TA Q600. When under flowing N_2 atmosphere, the samples were heated in a Platinum pan (800 °C, 10 °C min^{-1}) under a N_2 flux (60 mL min^{-1}).

Power X-ray diffraction (PXRD): PXRD patterns were collected on an X-ray diffraction (XRD) system (DX-27mini, China) using Cu Kα radiation.

Scanning electron microscopy (SEM): SEM images were collected using a GeminiSEM 500 system.

Transmission electron microscope (TEM): TEM images were obtained with a Tecnai G2 F30 STwin.

Sorption isotherm for N_2: Micrometrics ASAP2040 system were used to measure the specific surface area and pore structure using nitrogen as the adsorbate at 77 K, after outgassing the samples overnight at 120 °C.

Gas sorption: The samples were activated under vacuum for 12 hours at 120 °C. Gas adsorption experiments at 298 K were performed by using JW-BK200 surface area analyzer. A circulation constant temperature water bath was used to stabilize the temperature at 298 K during the test.

Crystal structure modeling: Crystal structure modeling: The unit cell parameters of the COFs were obtained from the indexing of the PXRD peaks using the Dicvol (Reflex module in the Materials Studio program)[1], the structural modeling of COFs was generated using the Building (Crystal)

module, the lattice model was geometrically optimized using force-filed based method (Forcite molecular dynamics module). The Pawley fitting (Reflex module) was performed to optimize the lattice parameters iteratively until the *R*wp value converges and the overlay of the observed with refined profiles shows good agreement.

Calculation of selectivity via ideal adsorption solution theory (IAST):

The gas adsorption isotherms were first fitted to a dual-site Langmuir-Freundlich (DSLF) model (eqn (3)), where is the amount of adsorbed gas q (mmol g^{-1}), P is the bulk gas phase pressure (atm), $qsat$ is the saturation amount (mmol g^{-1}), b is the Langmuir-Freundlich parameter ($atm^{-\alpha}$), and α is the Langmuir-Freundlich exponent (dimensionless) for two adsorption sites A and B indicating the presence of weak and strong adsorption sites.

$$q = q_{A,sat}\frac{b_A p}{1 + b_A p} + q_{B,sat}\frac{b_B p}{1 + b_B p} \quad (3)$$

IAST starts from the Raoult's Law type of relationship between the fluid and adsorbed phase (4) and (5), where $\mathcal{P}_i$ is the partial pressure of component i (atm), *P* is the total pressure (atm), and y_i and x_i represent mole fractions of component i in gas and the adsorbed phase (dimensionless). P_i^0 is the equilibrium vapour pressure (atm).

$$P_i = P y_i = P_i^0 x_i \quad (4)$$

$$\sum_{i=1}^{n} x_i = \sum_{i=1}^{n} \frac{P_i}{P_i^0} = 1 \quad (5)$$

In IAST, P is defined by relating to spreading pressure π (6), where π is the spreading pressure, S is the specific surface area of the adsorbent (m^2 g^{-1}), R is the gas constant (8.314 J K^{-1} mol^{-1}), T is the temperature (K), and $q_i(P_i)$ is the single component equilibrium obtained from isotherms (mmol g^{-1}).

$$\frac{\pi S}{RT} = \int_0^{p^0} i \frac{q_i(P_i)}{P_i} \mathbb{d} p_i = \Pi(condtant) \quad (6)$$

For a DSLF model, we have an analytical expression for the integral (7). The isotherm parameters are derived from the previous fitting. For a binary component system, the unknowns will be Π, P, and which can be obtained by simultaneously solving eqn (5) and (7).

$$\int_0^{p^0} i \frac{q_i(P_i)}{P_i} \mathbb{d} p_i = \Pi(condtant) = \frac{q_{sat,A}}{a_A} \ln\left[1 + b_A (P_i^0)^{a_A}\right] + \frac{q_{sat,B}}{a_B} \ln\left[1 + b_B (P_i^0)^{a_B}\right] \quad (7)$$

The adsorbed amount of each compound in a mixture is (8) and (9), where q is the adsorbed amount of component (mmol g^{-1}), and is the total adsorbed amount (mmol g^{-1}).

$$q_i^{mix} = x_i q_t \quad (8)$$

$$\frac{1}{q_T} = \sum_{i=1}^{n} \frac{x_i}{q_i(P_i^0)} \quad (9)$$

The adsorption selectivities S_{ads} were calculated using eqn (10). In this study, IAST calculations were carried out assuming a binary mixed gas with a molar ratio of 50:50 at 298 K and pressures up to 1 atm.

$$S_{ads} = \frac{q_1/q_2}{p_1/p_2} \quad (10)$$

Isosteric heat of adsorption (Q_{st}):

The isosteric heats of adsorption were calculated using the Clausius-Clapeyron equation:

$$Q_{st} = -R \times \left[\frac{\partial ln(P)}{\partial(\frac{1}{T})}\right] \quad (11)$$

Where *R* is the gas constant constant (8.314 J·mol^{-1}·K^{-1}). Values of Qst were derived from the slopes of lnP versus 1/T plots at different adsorption loadings:

$$Q_{st} = -slope \times R \quad (12)$$

Dynamic Breakthrough experiments:

The breakthrough separation experiment was conducted in a home-built breakthrough apparatus under ambient conditions (298 K, 1 bar). In a typical breakthrough experiment, the activated Cu-HAPB (0.3 g) and Cu-HABPB (about 0.34 g) powders were packed into stainless steel column (Φ 6 × 80 mm) and purged with He flow (20 mL/min) for 4 hours at 298 K for the activation process.

2. Synthesis and characterization

2.1. Synthesis of monomers

Scheme S1 Synthesis of Cu(I)-cluster aldehyde. $Cu_3(PA)_3$ was prepared according to a previously reported procedure[2]. $Cu(NO_3)_2{\cdot}3H_2O$ (0.20 g, 0.83 mmol) and 1H-pyrazole-4-carbaldehyde (HPyCA, 0.096 g, 1.0 mmol) were dissolved in a mixed solvent of N, N-dimethylformamide (DMF, 6.7mL), water (5.0 mL), and ethanol (6.7 mL) in a 25 mL sealed flask. The reaction mixture was heated at 100 °C for 12 h, affording white needle-like crystals. The product was collected by filtration, washed thoroughly with ethanol, and dried under vacuum at 50 °C for 12 h to give the final crystalline Cu(I)-cluster aldehyde (yield: 67%).

2.2 Synthesis of Cu-HAPB and Cu-HABPB

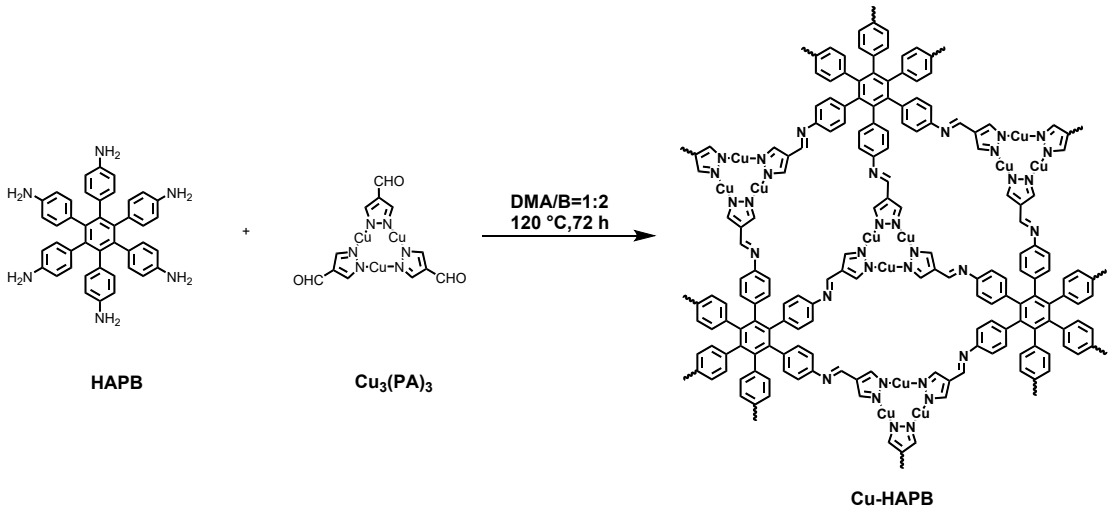

Scheme S2. Synthesis of Cu-HAPB: In a 10 mL Pyrex test tube, HAPB (18.72 mg, 0.03 mmol) and $Cu_3(PA)_3$ (28.5 mg, 0.06 mmol) were added to a solvent mixture of N,N-dimethylacetamide (DMAc, 0.4 mL) and *n*-butanol (0.8 mL). The suspension was sonicated for 5 min to form a homogeneous grey dispersion, followed by addition of 0.12 mL of 9 M acetic acid as catalyst. The reaction mixture was frozen at 77 K, degassed via three freeze-pump-thaw cycles, and flame-sealed under vacuum. The sealed tube was then heated at 120 °C for 3 days. After cooling to room temperature, the resulting precipitate was collected by centrifugation (6000 rpm, 3 min), washed with anhydrous acetone, and subjected to solvent exchange with anhydrous tetrahydrofuran. The solid was finally vacuum-dried at 80 °C for 12 h to afford Cu-HAPB as a green powder (35.4 mg, 75.3% yield).

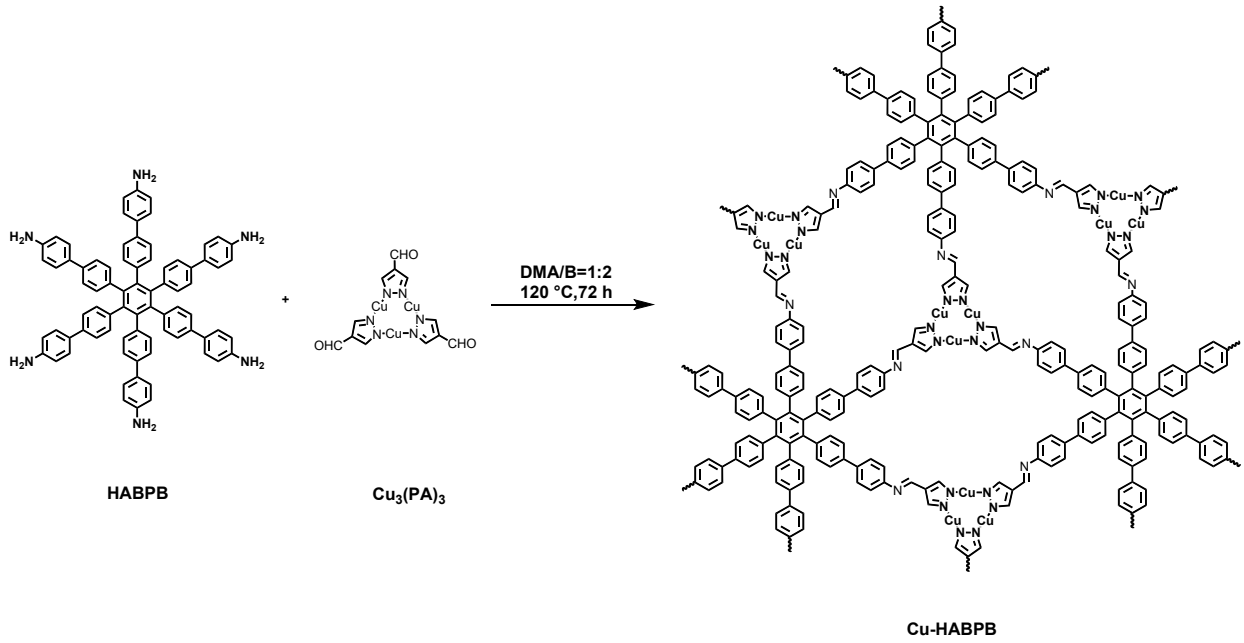

Scheme S3. Synthesis of Cu-HABPB: In a 10 mL Pyrex test tube, HABPB (21.5 mg, 0.02 mmol) and $Cu_3(PA)_3$ (19 mg, 0.04 mmol) were added to a solvent mixture of N,N-dimethylacetamide (DMAc, 0.4 mL) and *n*-butanol (0.8 mL). The suspension was sonicated for 5 min to form a homogeneous grey dispersion, followed by addition of 0.12 mL of 9 M acetic acid as catalyst. The reaction mixture was frozen at 77 K, degassed via three freeze-pump-thaw cycles, and flame-sealed under vacuum. The sealed tube was then heated at 120 °C for 3 days. After cooling to room temperature, the resulting precipitate was collected by centrifugation (6000 rpm, 3 min), washed with anhydrous acetone, and subjected to solvent exchange with anhydrous tetrahydrofuran. The solid was finally vacuum-dried at 80 °C for 12 h to afford Cu-HAPB as a green powder (29.5 mg, 72.8% yield).

2.3. Characterization of Cu-HAPB and Cu-HABPB

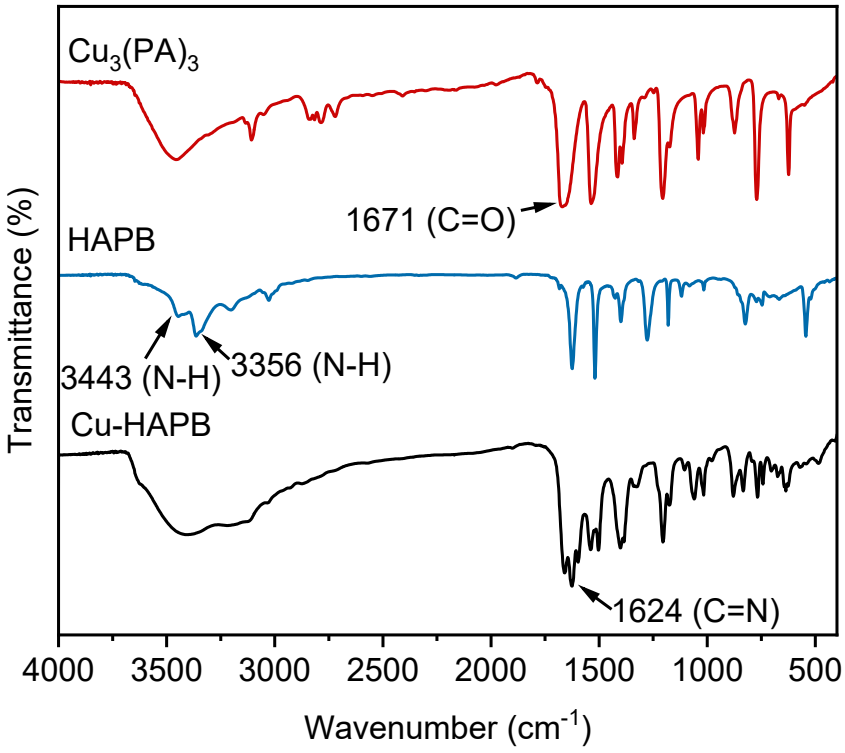

Figure S1. FT-IR spectra of $Cu_3(PA)_3$, HAPB, and Cu-HAPB.

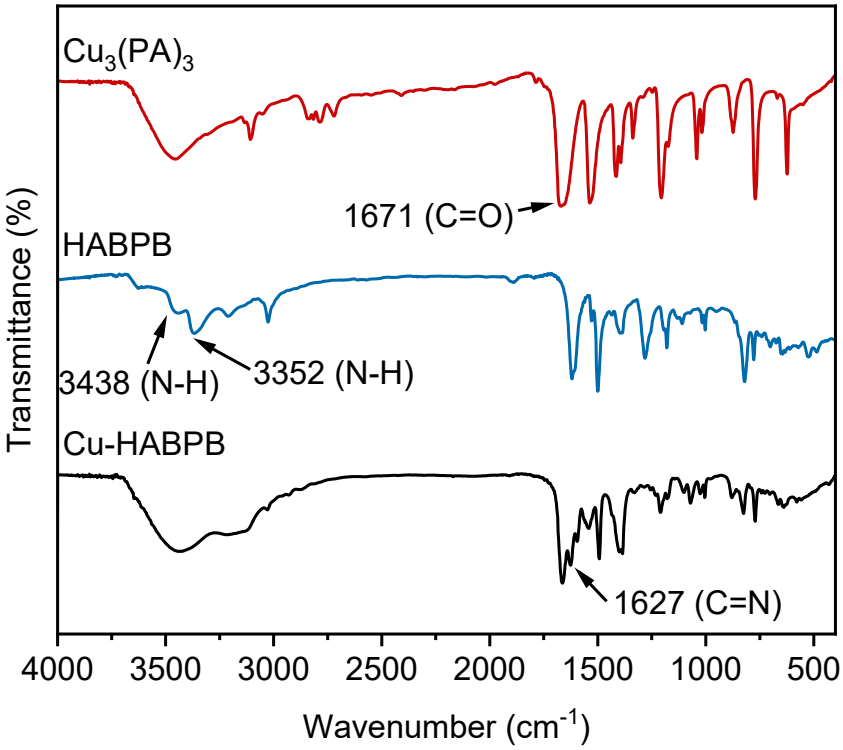

Figure S2. FT-IR spectra of $Cu_3(PA)_3$, HABPB, and Cu-HABPB.

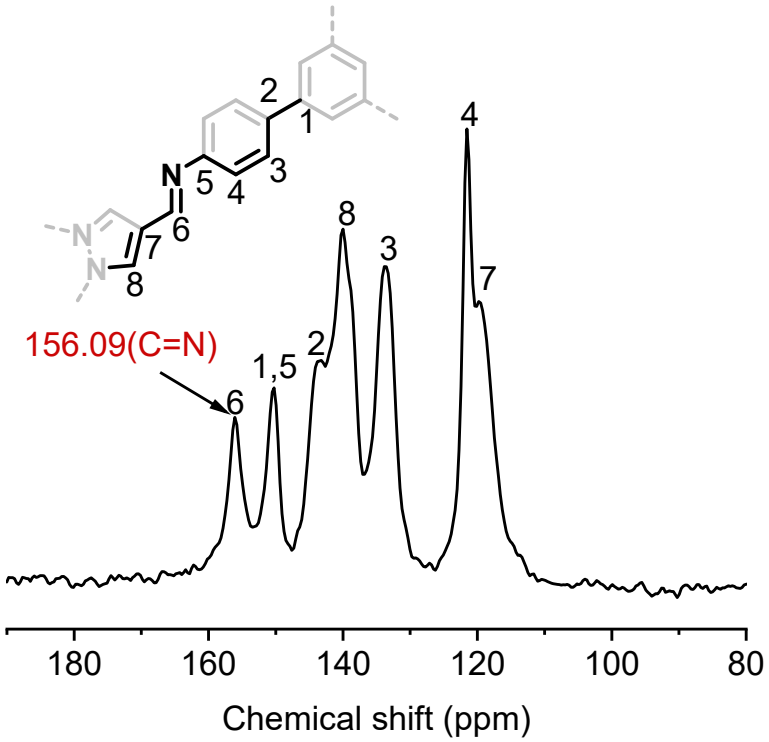

Figure S3. Solid-state ^{13}C CP/MAS NMR spectrum of Cu-HAPB.

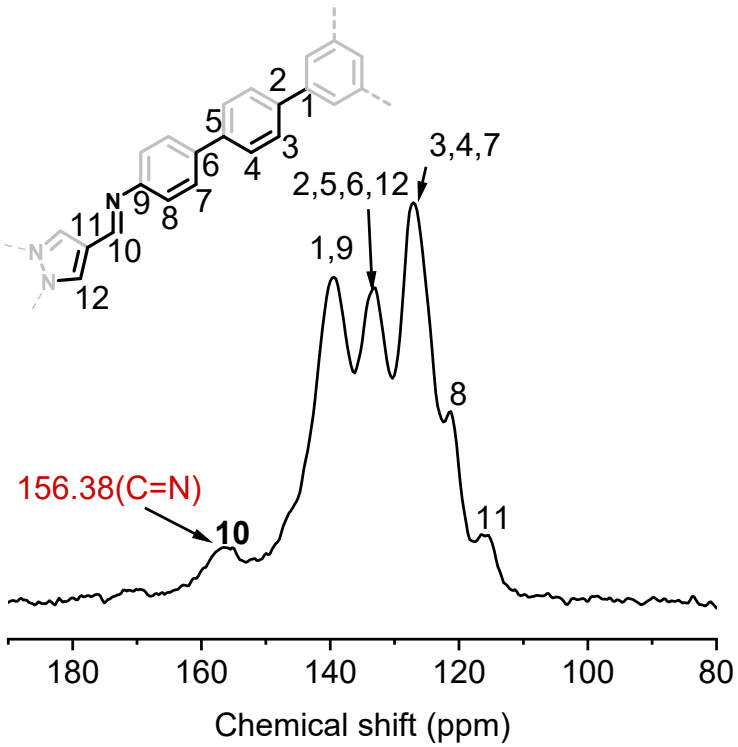

Figure S4. Solid-state ^{13}C CP/MAS NMR spectrum of Cu-HABPB.

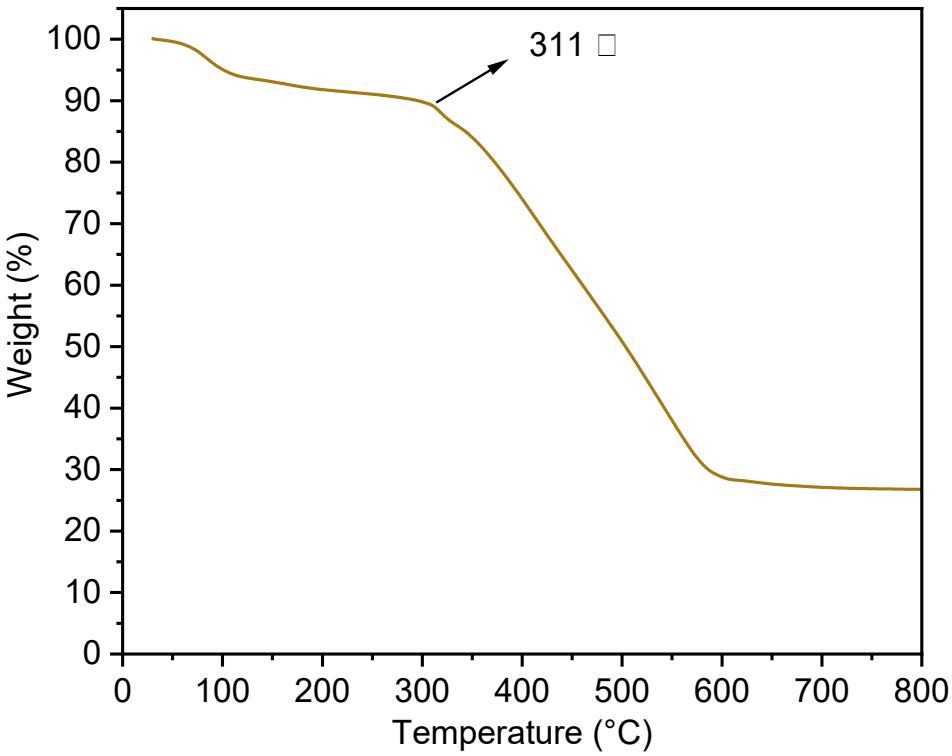

Figure S5. TGA curve of Cu-HAPB under N_2 atmosphere conditions.

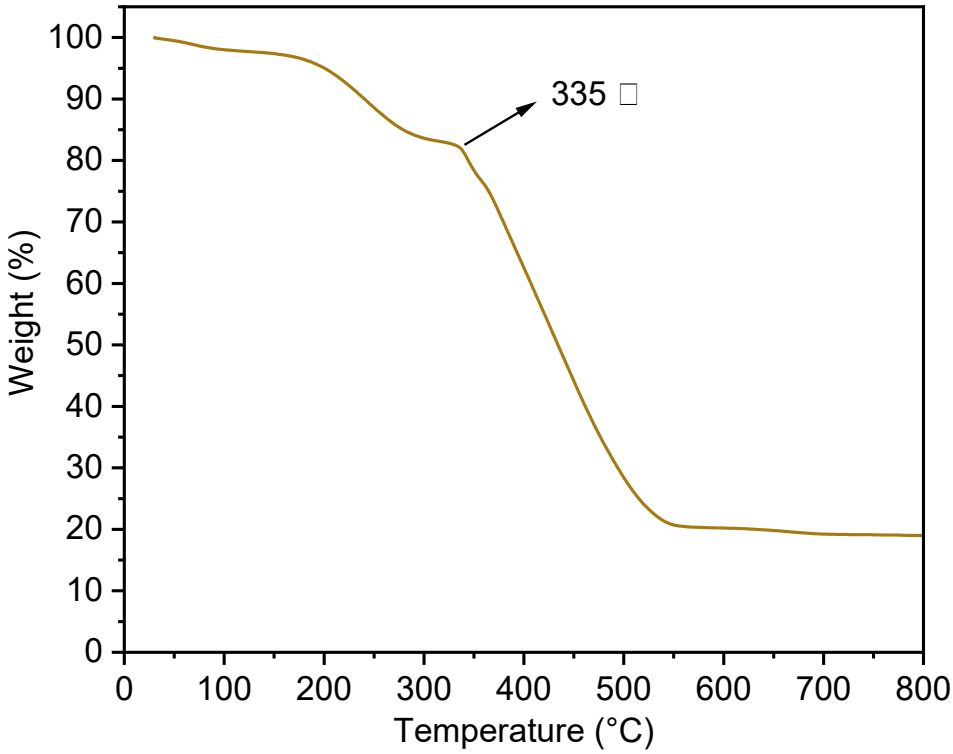

Figure S6. TGA curve of Cu-HABPB under N_2 atmosphere conditions.

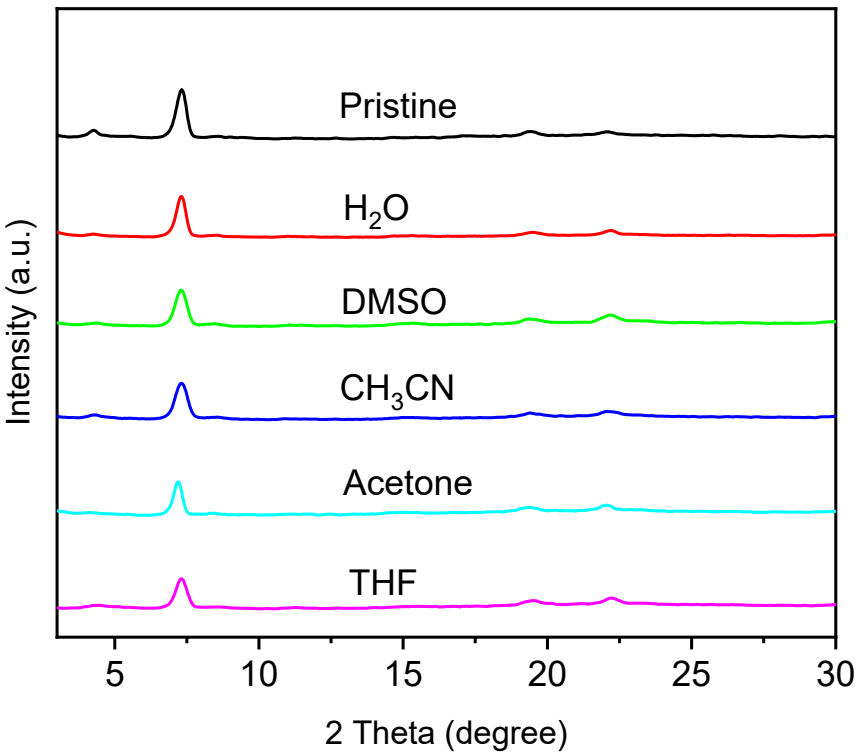

Figure S7. PXRD patterns of Cu-HAPB after immersion in various solvents for 72 hours, demonstrating its structural stability.

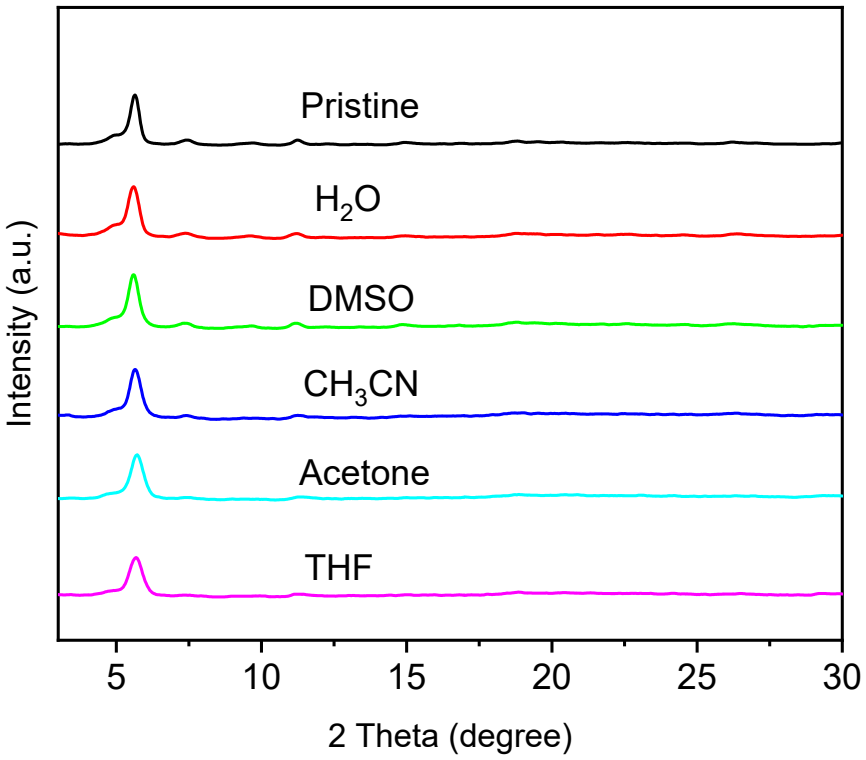

Figure S8. PXRD patterns of Cu-HABPB after immersion in various solvents for 72 hours, demonstrating its structural stability.

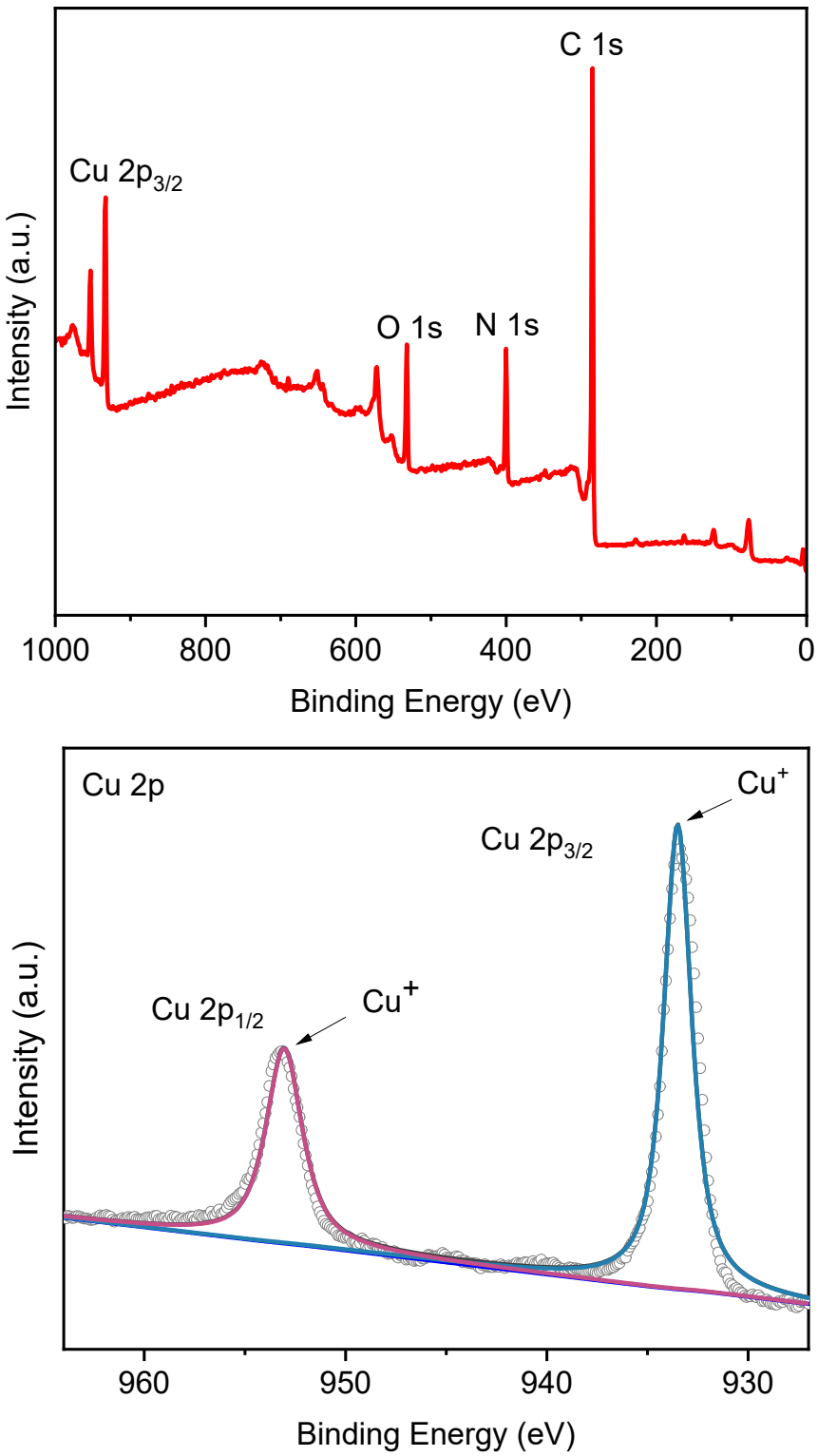

Figure S9. XPS survey scan and Cu 2p spectra for Cu-HAPB.

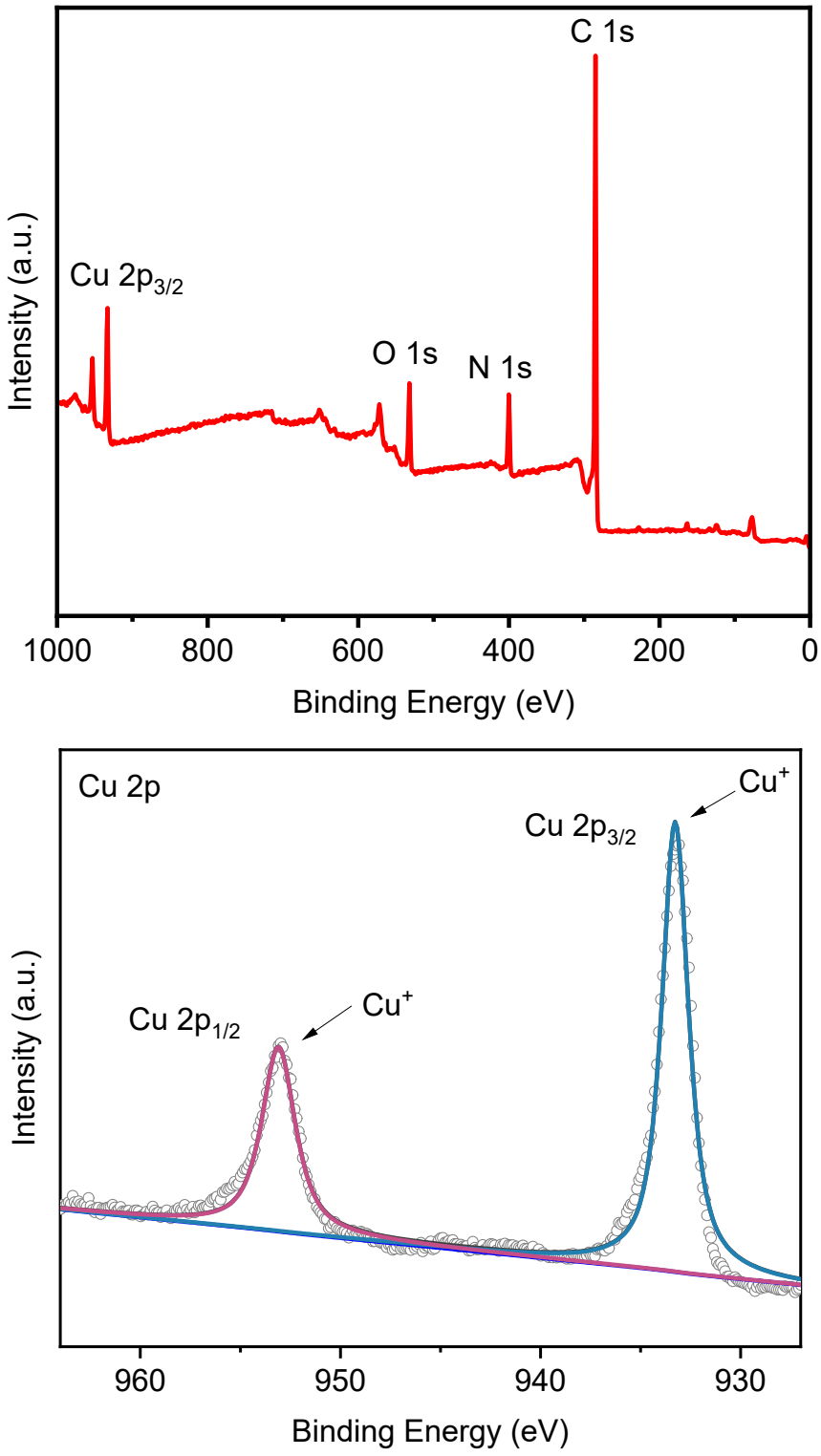

Figure S10 . XPS survey scan and Cu 2p spectra for Cu-HABPB.

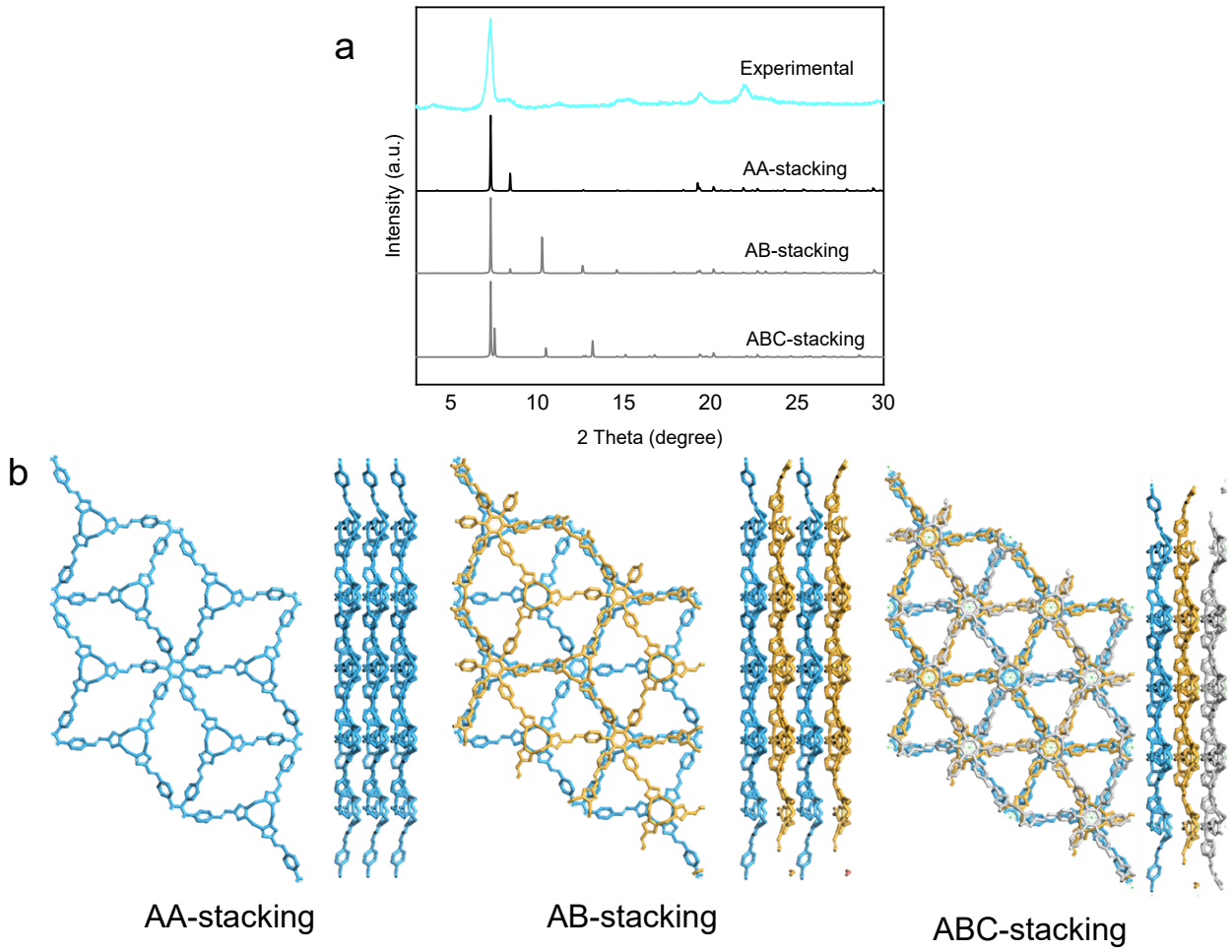

Figure S11. (a) PXRD patterns of Cu-HAPB: comparison of the experimental profile with simulated patterns based on AA, AB, and ABC stacking models. (b) Structural models of Cu-HAPB illustrating the AA, AB, and ABC stacking arrangements.

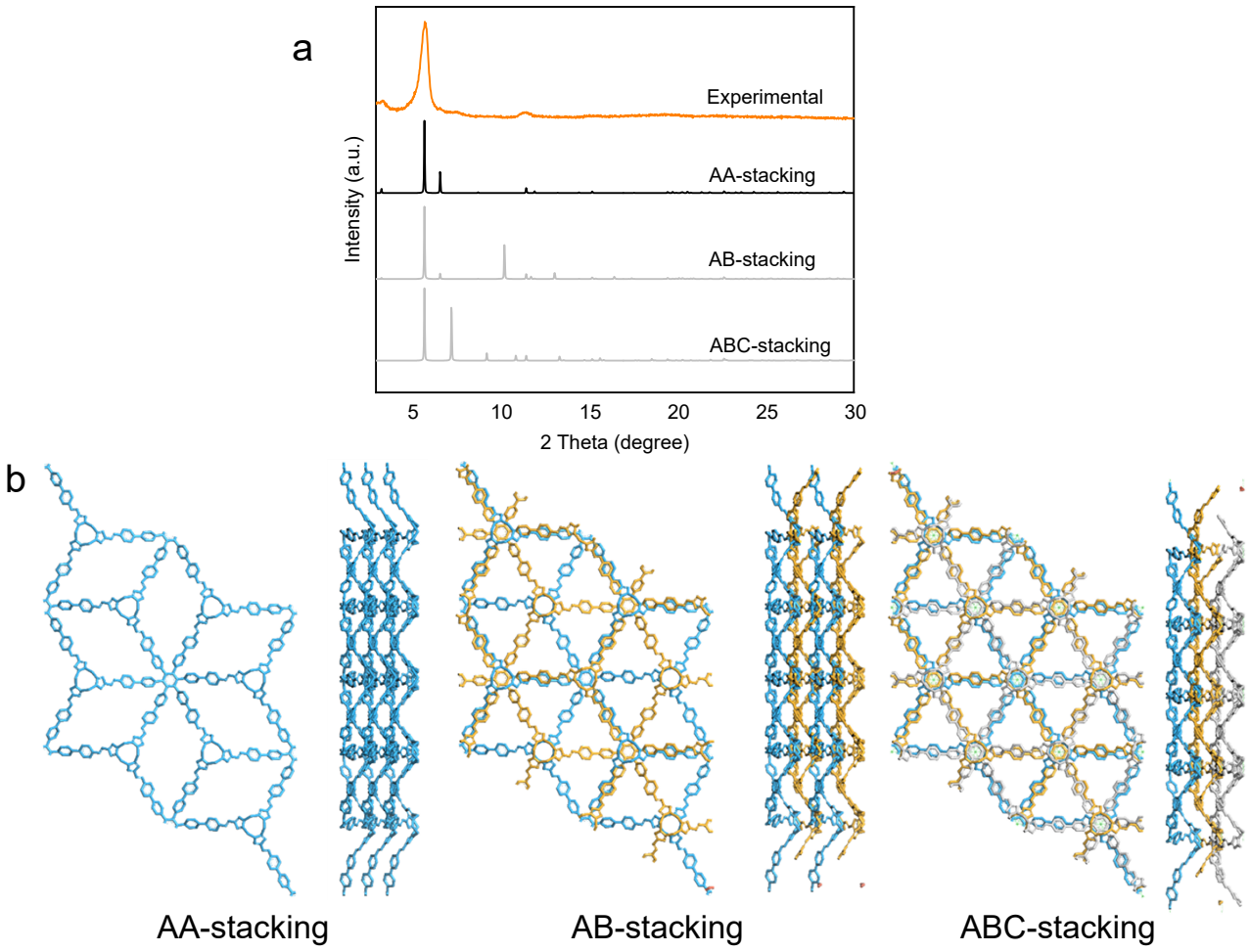

Figure S12. (a) PXRD patterns of Cu-HABPB: comparison of the experimental profile with simulated patterns based on AA, AB, and ABC stacking models. (b) Structural models of Cu-HABPB illustrating the AA, AB, and ABC stacking arrangements.

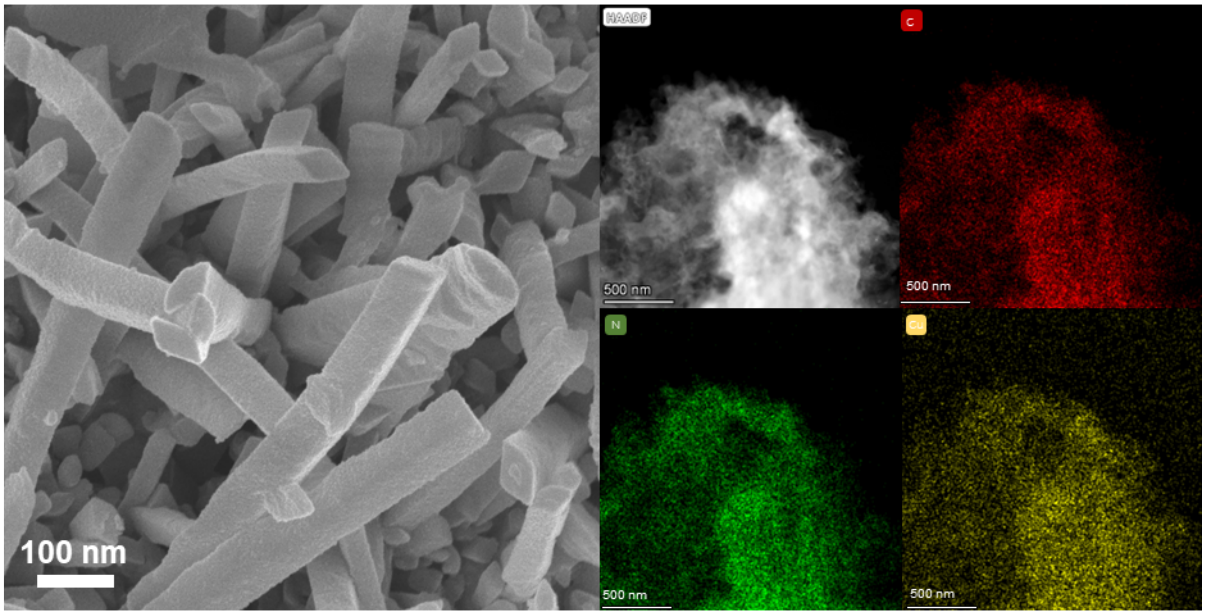

Figure S13. SEM image and TEM elemental mapping of Cu-HAPB.

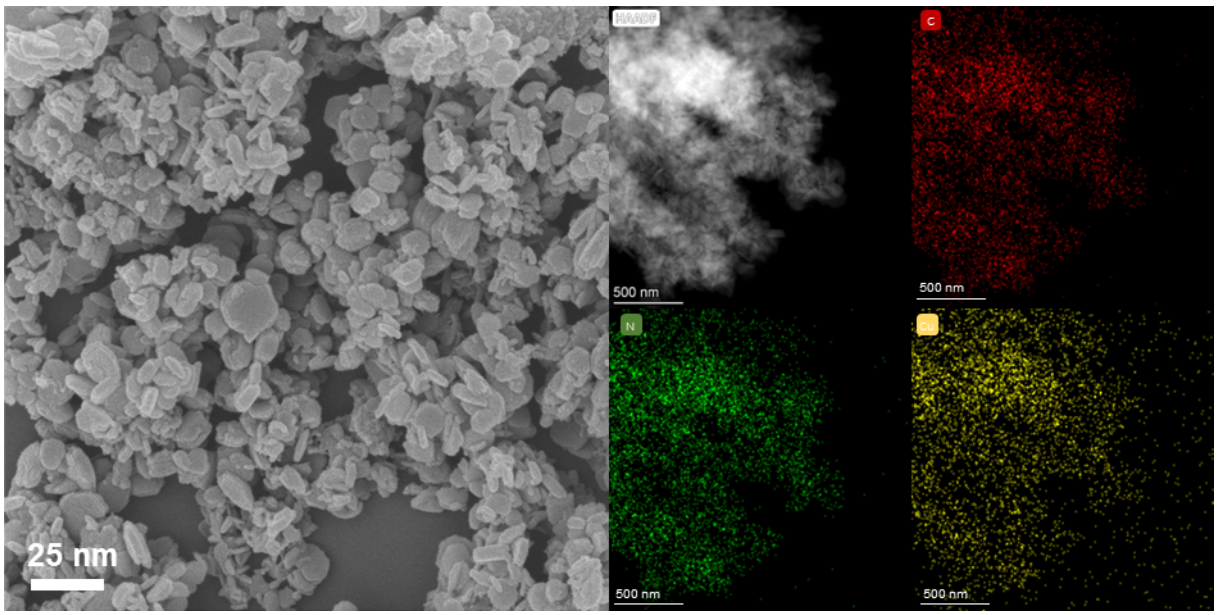

Figure S14. SEM image and TEM elemental mapping of Cu-HABPB.

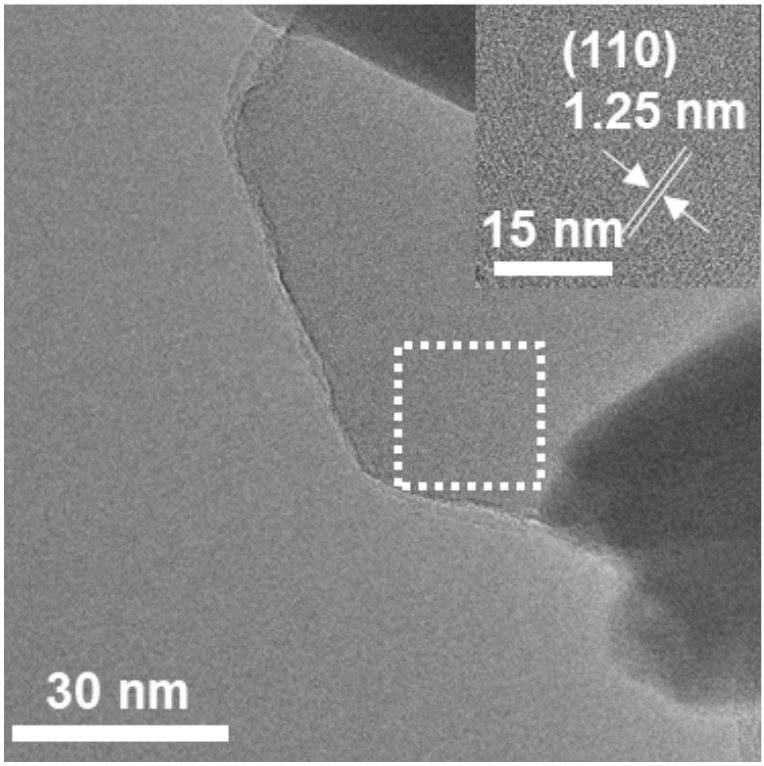

Figure S15. TEM image of Cu-HAPB, showing lattice fringes with an interlayer spacing of 1.25 nm indexed to the (110) crystallographic plane.

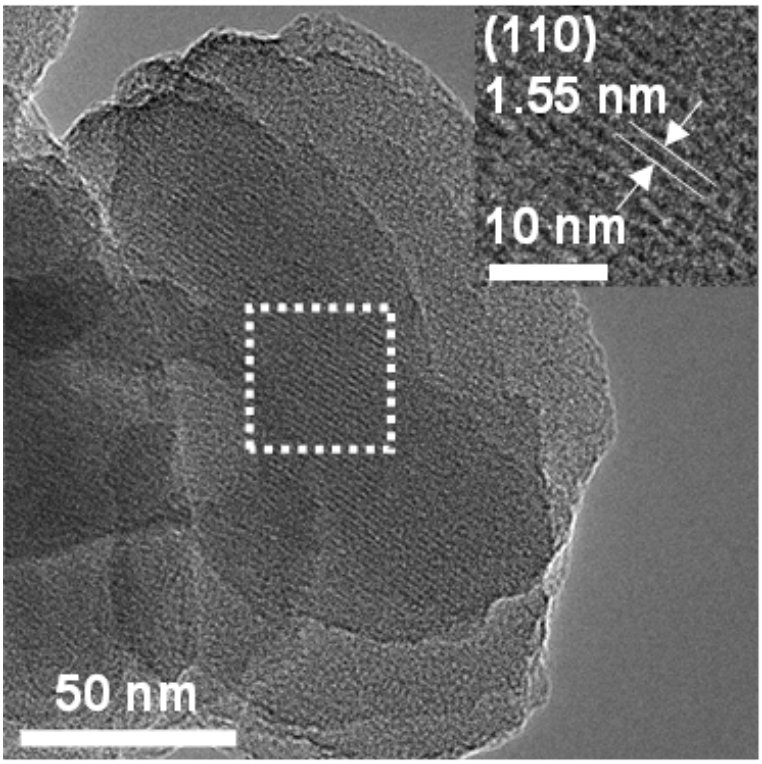

Figure S16. TEM image of Cu-HABPB, showing lattice fringes with an interlayer spacing of 1.55 nm indexed to the (110) crystallographic plane.

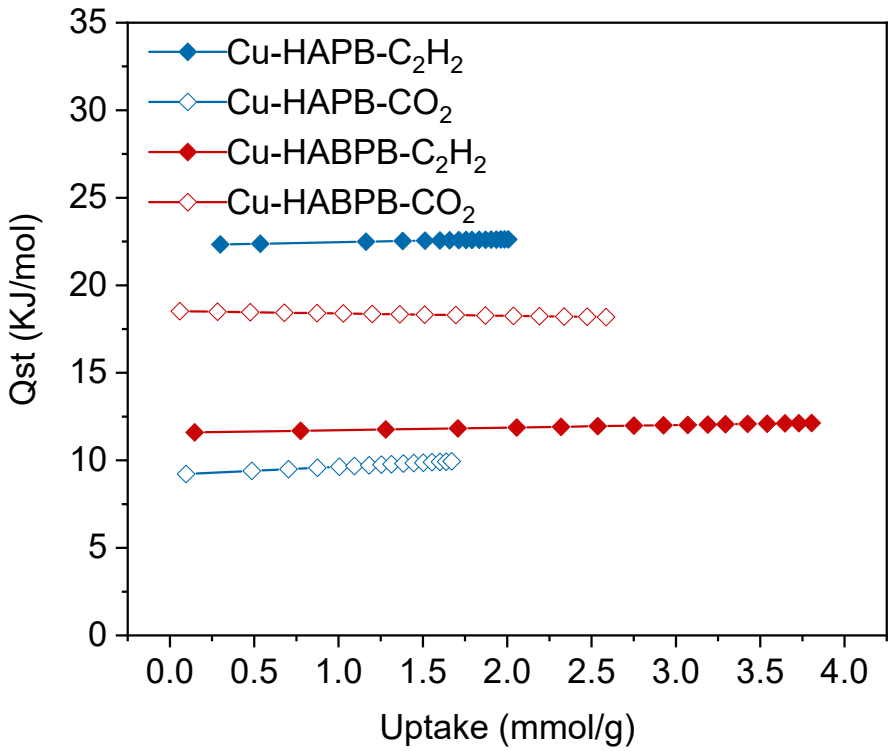

Figure S17. Coverage-dependent isosteric heats of adsorption (Q_{st}) for C_2H_2 and CO_2 in Cu-HAPB and Cu-HABPB.

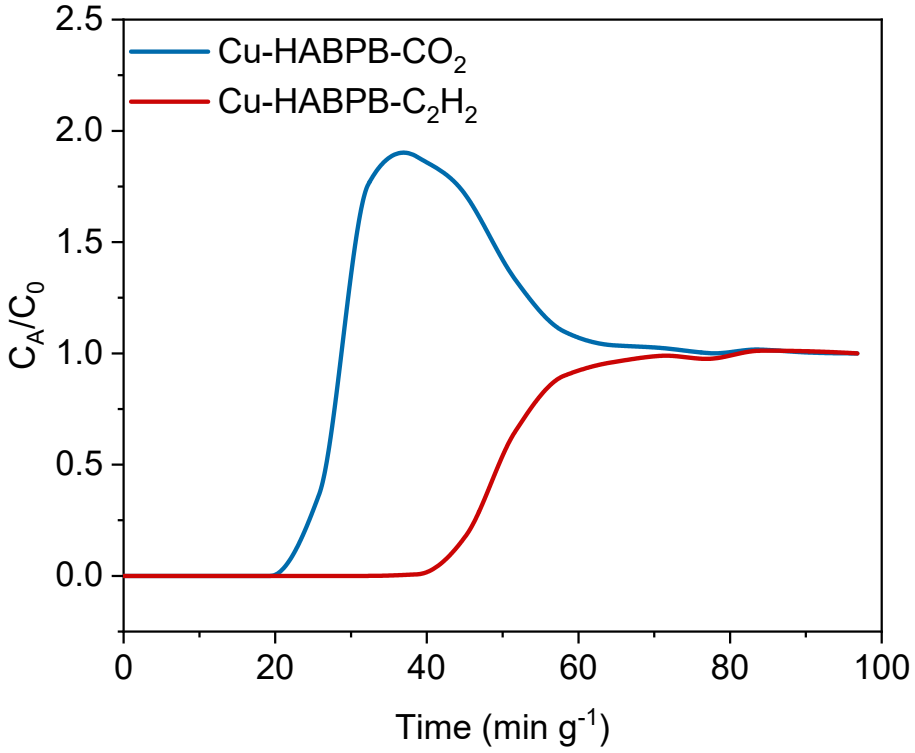

Figure S18. Dynamic breakthrough curves for C_2H_2/CO_2 separation on Cu-HABPB at 298 K under a total flow rate of 1.0 mL min^{-1}.

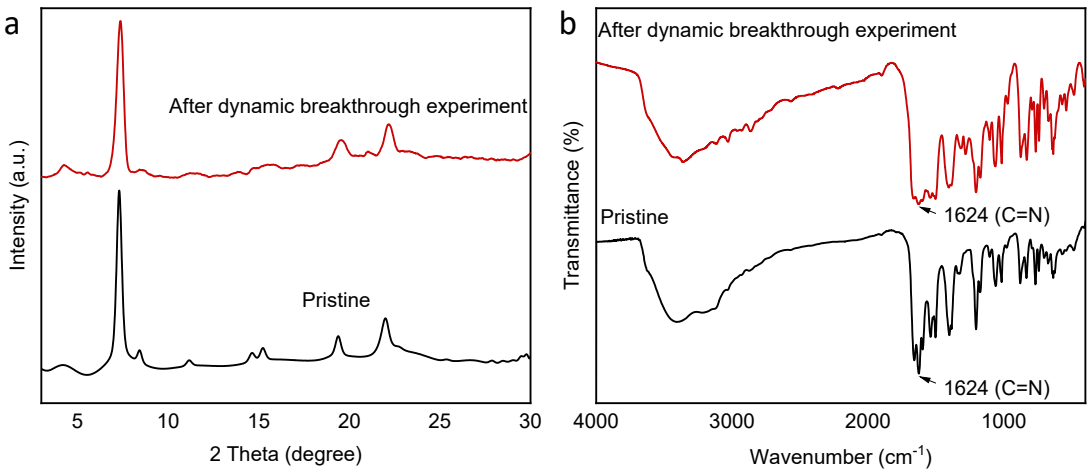

Figure S19. (a) PXRD patterns and (b) FT-IR spectra of Cu-HAPB before and after the dynamic breakthrough experiment.

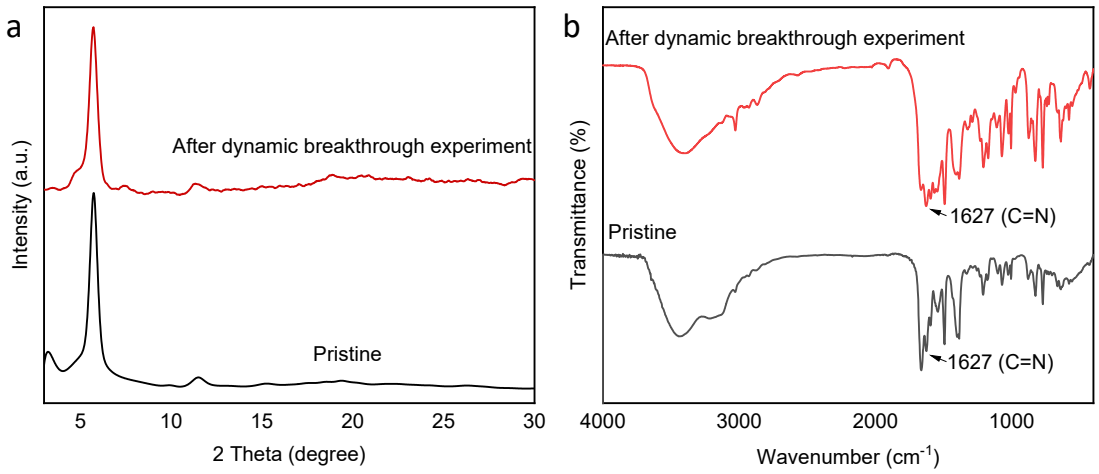

Figure S20. (a) PXRD patterns and (b) FT-IR spectra of Cu-HABPB before and after the dynamic breakthrough experiment.

Table S1. Unit cell parameters and fractional atomic coordinates of Cu-HAPB derived from structural optimization based on AA stacking with kgd topology.

Space group		*P*6	
Calculated unit cell		*a* = 24.2256 Å, *b* = 24.2256 Å, *c* = 4.7216 Å *α* = 90.0000°, *β* = 90.0000°, *γ* = 120.0000°	
Atoms	X	Y	Z
C1	4.03906	1.06972	-0.71884
C2	4.08412	1.14375	-0.68506
C3	4.13049	1.16848	-0.46219
C4	4.17011	1.23701	-0.41619
C5	4.16237	1.28233	-0.5843
C6	4.11596	1.25852	-0.80737
C7	4.07778	1.18966	-0.85949
N8	4.19895	1.3515	-0.50856
N9	4.24014	1.55549	-0.24357
C10	4.1912	1.50203	-0.37866
C11	4.21764	1.46238	-0.45787
C12	4.28258	1.49295	-0.35756
N13	4.29456	1.55024	-0.23321
Cu14	4.37464	1.60927	-0.01617
C15	4.17877	1.3936	-0.56192
C1	4.03906	1.06972	-0.71884
C2	4.08412	1.14375	-0.68506
C3	4.13049	1.16848	-0.46219
C4	4.17011	1.23701	-0.41619
C5	4.16237	1.28233	-0.5843

Table S2. Unit cell parameters and fractional atomic coordinates of Cu-HABPB derived from structural optimization based on AA stacking with kgd topology.

Space group		*P*6	
Calculated unit cell		*a* = 30.8000 Å, *b* = 30.8000 Å, *c* = 4.5549 Å *α* = 90.0000°, *β* = 90.0000°, *γ* = 120.0000°	
Atoms	X	Y	Z
C1	4.94326	0.96637	-1.0363
C2	4.88391	0.93122	-1.00225
C3	4.84745	0.93802	-1.17388
C4	4.79253	0.90867	-1.11547
C5	4.77214	0.87053	-0.88946
C6	4.80723	0.8615	-0.71964
C7	4.86205	0.89105	-0.76481
C8	4.71495	0.84345	-0.80824
C9	4.684	0.86748	-0.86642
C10	4.63213	0.84538	-0.75386
C11	4.61035	0.79879	-0.58419
C12	4.64072	0.77394	-0.53235
C13	4.69254	0.79619	-0.64252
N14	4.55981	0.7803	-0.4429
N15	4.41649	0.67172	0.13656
C16	4.45311	0.66818	-0.02884
C17	4.48558	0.71828	-0.14651
C18	4.46772	0.75154	-0.04126
N19	4.42525	0.7212	0.1304
Cu20	4.38582	0.74629	0.36847
C21	4.53431	0.73412	-0.31512
C1	4.94326	0.96637	-1.0363

Table S3. Summary of C_2H_2 and CO_2 adsorption capacities and C_2H_2/CO_2 (50/50, v/v) IAST selectivities for various porous materials at 298 K and 100 kPa.

Porous materials	**q, C_2H_2 ($cm^3 \cdot g^{-1}$)**	**q, CO_2 ($cm^3 \cdot g^{-1}$)**	**C_2H_2/CO_2 selectivity**	**Refs.**
Cu-HAPB	43.28	30.74	6.23	This work
Cu-HABPB	72.32	40.95	3.39	This work
UPC-COF-1	89.8	45.5	4.5	3
TPZ-COF	107.21	63.42	3.1	4
NUS-71	42.4	10.3	16	5
JUC-662	65.1	31.2	3.3	6
2D sql COF	77.8	39.4	4.8	7
Zn-btb-dmtrz	86.0	38.1	2.7	8
FJU-90a	180.0	103.0	4.3	9
USTB-25-3D	77.28	39.23	6.34	10
Cu^{I}@MOF 303	193.4	114.6	1.69	11
HOF-FJU-1	43	12.4	3.46	12
KUF-5	30.48	6.40	4.8	13

References

1. Materials Studio; Accelrys: San Diego.
2. X. Li, J. Wang, F. Xue, Y. Wu, H. Xu, T. Yi and Q. Li, *Angew. Chem. Int. Ed.*, 2021, **133**, 2564-2570.
3. X. Wang, H. Liu, M. Sun, F. Gao, X. Feng, M.Xu, W. Fan and D. Sun, *Angew. Chem. Int. Ed.*,2025 , **137**, e202420801.
4. M. Yang, S. Qiao, J. Wang, P. Shi, and Z. Guo, *Small*, 2026, e12337.
5. Z. Zhang, C. Kang, S. Peh, D. Shi, F. Yang, Q. Liu, and D. Zhao, *J.Am.Chem.Soc.*, 2022, **144**, 14992-14996.
6. J. Zhang, H. Zheng, F. Chen, Z. Wang, H. Li, F. Sun, D. Zhao, V. Valtchev, S. Qiu and Q. Fang, *Angew. Chem. Int. Ed.*,2025, **64**, e202500161.
7. L. Chen, C. Gong, X. Wang, F. Dai, M. Huang, X. Wu, C. Lu, and Y. Peng, *J.Am.Chem.Soc.*, 2021, **143**, 10243-10249.
8. C. Lu, S. Liu, Z. Wang, X. Wei, X. Chen, X. Wang, J. Pang, S. Geng, X. Lu, J. Duan, F. Dai and X. Bu, *Adv. Mater.*, 2026, **38**, e14488.
9. Y. Ye, Z. Ma, R. Lin, R. Krishna, W. Zhou, Q. Lin, Z. Zhang, S. Xiang and B. Chen, *J.Am.Chem.Soc.* ,2019, **141**, 4130-4136.
10. C. Jiang, C. Hao, X. Wang, H. Liu, X. Wei, H. Xu, Z. Wang, Y. Ouyang, W. Guo, F. Dai and D. Sun, *Chem. Eng. J.*,2023, **453**, 139713.
11. Z. Jiang, W. Wang, W. Xue, H. Zhu, M. Zheng, H. Huang and C. Zhong, Sep. *Purif. Technol.*, 2023, **322**, 124345.
12. Y. Yang, H. Zhang, Z. Yuan, J. Wang, F. Xiang, L. Chen, F. Wei, S. Xiang, B. Chen, and Z. Zhang, *Angew. Chem. Int. Ed.*,2022, **134**, e202207579.
13. Y. Lee, N.Kim, H. Yun, H. Kim, J. Choe and C. Hong, *ACS Appl. Mater. Interfaces.*, 2025. **17**, 45226-45233.